CHEMISTRY OF MATERIALS

Article

pubs.acs.org/cm

Design of Ternary Nanoalloy Catalysts: Effect of Nanoscale Alloying and Structural Perfection on Electrocatalytic Enhancement

Bridgid N. Wanjala,[†] Bin Fang,[†] Shiyao Shan,[†] Valeri Petkov,[‡] Pengyu Zhu,[§] Rameshwori Loukrakpam,[†] Yongsheng Chen,[§] Jin Luo,[†] Jun Yin,[†] Lefu Yang,[†] Minhua Shao,[⊥] and Chuan-Jian Zhong*[,†]

[†]Department of Chemistry, State University of New York at Binghamton, Binghamton, New York 13902, United States

[‡]Department of Physics, Central Michigan University, Mt. Pleasant, Michigan 48859, United States

[§]EMS Energy Institute, Department of Energy and Mineral Engineering, and Materials Research Institute, Pennsylvania State University, University Park, Pennsylvania 16802, United States

[⊥]UTC Power, 195 Governor's Highway, South Windsor, Connecticut 06074, United States

Supporting Information

ABSTRACT: The ability to tune the atomic-scale structural and chemical ordering in nanoalloy catalysts is essential for achieving the ultimate goal of high activity and stability of catalyst by design. This article demonstrates this ability with a ternary nanoalloy of platinum with vanadium and cobalt for oxygen reduction reaction in fuel cells. The strategy is to enable nanoscale alloying and structural perfection through oxidative−reductive thermochemical treatments. The structural manipulation is shown to produce a significant enhancement in the electrocatalytic activity of the ternary nanoalloy catalysts for oxygen reduction reaction. Mass activities as high as 1 A/mg of Pt have been achieved by this strategy based on direct measurements of the kinetic currents from rotating disk electrode data. Using a synchrotron high-energy X-ray diffraction technique coupled with atomic pair function analysis and X-ray absorption fine structure spectroscopy as well as X-ray photoelectron spectroscopy, the atomic-scale structural and chemical ordering in nanoalloy catalysts prepared by the oxidative−reductive thermochemical treatments were examined. A phase transition has been observed, showing an fcc-type structure of the as-prepared and the lower-temperature-treated particles into an fct-type structure for the particles treated at the higher temperature. The results reveal a thermochemically driven evolution of the nanoalloys from a chemically disordered state into chemically ordered state with an enhanced degree of alloying. The increase in the chemical ordering and shrinking of interatomic distances as a result of thermochemical treatment at increased temperature is shown to increase the catalytic activity for oxygen reduction reaction, exhibiting an optimal activity at 600 °C. It is the alloying and structural perfection that allows the optimization of the catalytic performance in a controllable way, highlighting the significant role of atomic-scale structural and chemical ordering in the design of nanoalloy catalysts.

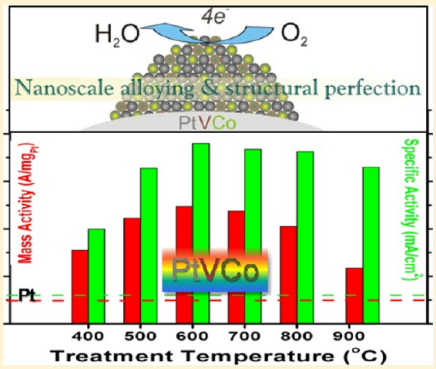

KEYWORDS: *nanoalloy, ternary catalysts, oxygen reduction reaction, chemical ordering, nanoscale alloying, and electrocatalysts*

INTRODUCTION

Although alloying Pt with different transition metals has been an actively explored area of research for developing active, robust, and low-cost catalysts for oxygen reduction reaction (ORR) in fuel cells,[1] the understanding of the enhanced electrocatalytic activity has been largely limited to factors such as changes in Pt−Pt interatomic distances, d-band center shift, Pt skin effect, etc.[2−6] Similar to the most studied pure Pt catalyst,[7−11] the particle size and shape have been reported to affect the electrocatalytic activity for binary[12,13] and ternary alloys of composition PtMM′ (where M and M′ are transition metals).[2,14−24] In particular, the introduction of two base metals (M′ and M = Co, Ni, etc.) to form ternary alloy PtMM′ electrocatalysts such as PtVFe, PtNiFe, PtNiCo, and PtIrCo[25−29] has recently been shown to exhibit a much higher electrocatalytic activity than that of pure Pt. In some cases, the activity has also been shown to be higher than those of the respective binary alloys for ORR.[2,30] In recent studies, computational work on the surface properties and dissolution trends of Pt_3Fe, Pt_3Co, and Pt_3Ni alloys in the presence of adsorbates[31] and XAFS measurements on local ordering changes in PtCo nanocatalyst induced by fuel cell working conditions[32] have demonstrated that the transition metals in the binary alloys take an active part in the electrochemical process. Despite these studies and the realization about additional synergistic effects on the activity due to differences in the redox potentials of M and M′ species, one important fundamental question remains unanswered about the design of the nanoalloy catalysts: What particular features of the atomic-scale structure in the nanoalloys correlate best with the

Received: May 24, 2012
Revised: September 5, 2012
Published: October 22, 2012

enhanced activity? Most of the previous studies have focused on achieving a so-called compromise between the particle's size and the electrochemically active surface area often considered in terms of crystallite's facets. There is a clear lack of understanding of the ability to tune the atomic-scale structural and chemical ordering in nanoalloy catalysts that is essential for achieving the ultimate goal of high activity and stability of catalyst by design.

In this study, PtVCo has been chosen as a ternary system based on some of the known facts from its bimetallic counterparts (PtV and PtCo),[2,30] which show enhanced electrocatalytic activities. The study focuses on unravelling the effect of thermochemical treatment temperature on the atomic-scale structure and chemical ordering/disordering and, hence, on the catalytic activity. This focus goes beyond the previous studies of binary/ternary alloys based on crystallite's facets and infinite lattice approximations that are, strictly speaking, not very precise descriptors of nanosized particles. As the results from synchrotron high energy X-ray diffraction (HE-XRD) and extended X-ray absorption fine structure (EXAFS) characterizations will show, the oxidative−reductive thermal annealing leads to controllable changes in atomic-scale alloying and structural perfection in the enhancement of electrocatalytic activity.

EXPERIMENTAL SECTION

Chemicals. Platinum(II) acetylacetonate ($Pt(acac)_2$, 97%) was purchased from Alfa Aesar. Cobalt(III) acetylacetonate ($Co(acac)_3$, 99.95%) was purchased from Strem Chemicals. Vanadyl acetylacetonate ($VO(acac)_2$, 98%), 1,2-hexadecanediol (90%), octyl ether ($[CH_3(CH_2)_7]_2O$, 99%), oleylamine (70%), oleic acid (99+%), and Nafion solution (5 wt %) were purchased from Aldrich. Optima grade perchloric acid, and other solvents, such as ethanol and hexane, were purchased from Fisher Scientific. All chemicals were used as received.

Synthesis and Preparation. The synthesis of PtVCo nanoparticles involved the reaction of three metal precursors—$Pt^{II}(acac)_2$, $V^{IV}O(acac)_2$, and $Co^{III}(acac)_3$—in controlled molar ratios, similar to the synthesis of other trimetallic nanoparticles in terms of procedure,[33] but different in terms of the control parameters. These metal precursors were dissolved in octyl ether solvent. A mixture of oleylamine and oleic acid was also dissolved in the solution and used as capping agents. 1,2-Hexadecanediol was used as a reducing agent for the reduction of the Pt, V, and Co precursors. The formation of the oleylamine/oleic acid-capped PtVCo nanoparticles involves a combination of thermal decomposition and reduction reactions. The composition of the $Pt_{n1}V_{n2}Co_{n3}$ nanoparticles, where $n1$, $n2$, and $n3$ represent the atomic percentages of each metal, is controlled by the feeding ratio of the metal precursors. In a typical procedure for the synthesis of $Pt_{45}V_{18}Co_{37}$, for example, 1,2-hexadecanediol (2.5 mmol), $Pt(acac)_2$ (1.97 mmol), $VO(acac)_2$ (0.935 mmol), $Co(acac)_3$ (1.934 mmol), oleylamine (2.13 mmol), and oleic acid (3.13 mmol) were mixed in 120 mL octyl ether in a three-neck, 1 L flask under stirring. The solution was first purged with N_2 and heated to 105 °C and then heated to 270 °C and refluxed for 40 min. After the reaction mixture was allowed to cool to room temperature, the product was precipitated by adding ethanol. The black precipitate was completely dried under nitrogen and dispersed in a known amount of hexane.

The catalyst preparation included the assembly of PtVCo nanoparticles on carbon black and postsynthesis thermal treatment. The assembly was accomplished by a process of loading the nanoparticles onto carbon black materials through interactions between the capping shells and the carbon surface. A typical procedure (e.g., $Pt_{45}V_{18}Co_{37}$) included the following steps: First, 800 mg carbon black (Ketjen Black) was suspended in 400 mL of hexane. After sonicating for ∼3 h, ∼200 mg $Pt_{45}V_{18}Co_{37}$ was added into the suspension. The suspension was sonicated for 5 min, followed by stirring for ∼15 h. The suspension was evaporated slowly for ∼8 h by purging N_2 while stirring. The powder was collected and dried under N_2.

The thermal treatment involved removal of organic shells and annealing of the alloy nanoparticles. All samples were treated in a tube furnace using a quartz tube. The PtVCo nanoparticles supported on carbon (PtVCo/C) were first heated at 260 °C in 10% O_2 for 30 min for removing the organic shells (oxidation ("O") treatment), as confirmed by FTIR and XPS analyses[17,34] and then treated at various temperatures in the range between 400 and 926 °C in 15% H_2 for 120 min (reductive ("H") treatment). A control sample was only heated at 260 °C in N_2 for 30 min for removing the organic shells and then treated at 400 °C in 15% H_2 for 120 min. There is usually a slight or insignificant change for the alloy composition after oxidative−reductive treatments for the nanocatalysts prepared by our method.[27] The composition of the as-synthesized nanoparticles determined by inductively coupled plasma−optical emission spectroscopy (ICP−OES) was used to represent the ternary composition. Note that the determination of the composition of the carbon-supported catalysts was affected by the inaccuracy caused by adsorption of metals in the carbon materials, which could not be released during the acid digestion.[27]

Measurements. As-obtained nanoparticles and catalysts, that is, particles loaded on carbon, were characterized using the following techniques:

Transmission electron microscopy (TEM) measurements were performed on two different instruments to obtain the catalysts' particle size and size distributions. One instrument was a JEOL JEM 2010F with an acceleration voltage of 200 kV and a routine point-to-point resolution of 0.194 nm, which was also used to provide high-resolution TEM images. The other was a Hitachi H-7000 electron microscope (100 kV). For the purpose of counting and determining particle sizes with the carbon support as the background, we found that the particle size determination using images obtained from a Hitachi H-7000 was, in fact, more effective than those obtained from a JEOL JEM 2010F because of a better contrast between the particles and the carbon support for the former. The nanoparticle samples dissolved in hexane or toluene solution were drop-cast onto a carbon-coated copper grid sample holder, followed by natural evaporation of the solvent at room temperature

Inductively coupled plasma−optical emission spectroscopy (ICP−OES) was used to analyze the nanoparticle composition. It was performed on a Perkin-Elmer 2000 DV ICP-OES with the following parameters: plasma, 18.0 L of $Ar_{(g)}$/min; auxiliary, 0.3 L of $Ar_{(g)}$/min; nebulizer, 0.73 L of $Ar_{(g)}$/min; power, 1500 W; and peristaltic pump rate, 1.40 mL/min. Reported values of <1.0 mg/L were analyzed using a Meinhardt nebulizer coupled to a cyclonic spray chamber to increase the analyte sensitivity with the following parameters: 18.0 L of $Ar_{(g)}$/min; auxiliary, 0.3 L of $Ar_{(g)}$/min; nebulizer, 0.63 L of $Ar_{(g)}$/min; power, 1500 W; and peristaltic pump rate, 1.00 mL/min. Elemental concentrations were determined by measuring one or more emission lines (in nm) to check for interferences of Pt, 214.423 and 203.646; V, 309.311; and Co, 238.892 and 228.616. The concentration of Pt was determined only using the emission line at 214.423 nm in the presence of Co due to spectral interferences.

The nanoparticles' samples were dissolved in concentrated aqua regia and then diluted to concentrations in the range of 1−50 ppm for the analysis. Multipoint calibration curves were made from the dissolved standards with concentrations from 0 to 50 ppm in the same acid matrix as the unknowns. Laboratory check standards were analyzed every 6 or 12 samples, and instrument recalibration was performed if check standards were not within ±5% of the initial concentration. The method detection limits were determined using 1.0 mg/L of the analyte in the same acid matrix and are reported in milligrams per liter as follows: Pt ≤ 0.040 and V, Co ≤ 0.022. The instrument reproducibility (n = 10) was determined using 1 mg/L elemental solutions ensuring an <±2% error margin for all three elements.

Thermogravimetric analysis (TGA) was performed on a Perkin-Elmer Pyris 1-TGA for determining the weight of the particles' organic shells and the metal loading of the catalysts as reported in this work.

dx.doi.org/10.1021/cm301613j | Chem. Mater. 2012, 24, 4283−4293

Typical samples weighed ~4 mg and were heated in a platinum pan under 20% O_2 at a rate of 10 °C/min.

In-house X-ray powder diffraction (XRD) was used to determine phase state and lattice constants of the nanoparticle as well as to obtain an XRD-based estimate for their sizes. XRD data were collected from 20° to 90° 2θ with a step size of 0.05° at room temperature on a Phillips X'pert PW 3040 MPD diffractometer using Cu Kα radiation (λ= 1.5418 Å) and a sealed Xe proportional detector. The XRD collected patterns were compared with the XRD database of the International Centre for Diffraction Data (ICDD).

Synchrotron high energy X-ray diffraction (HE-XRD) was carried out at the beamline 11IDC at the Advanced Photon Source at the Argonne National Laboratory using X-rays of energy 115 keV (λ = 0.1078 Å). Samples were sealed in glass capillaries, and data were collected with an Image plate detector. The diffraction data were reduced to the so-called structure factors, $S(q)$, and then Fourier-transformed to the corresponding atomic PDFs, $G(r)$, using the relationship: $G(r) = 2/\pi \int_{q=0}^{q_{max}} q[S(q) - 1] \sin(qr)\, dq$, where q_{max} = 25 Å^{-1} in the present experiments. The software RAD was used for this purpose.[35] Here, the wave vector q is defined as $q = 4\pi \sin(\theta)/\lambda$, where θ is half of the scattering angle and λ is the wavelength of the X-rays used. Note, as derived, atomic PDFs $G(r)$ is an experimental quantity that oscillates around zero and shows positive peaks at real space distances, r, where the local atomic density $\rho(r)$ exceeds the average one, ρ_0. This behavior can be expressed by the equation $G(r) = 4\pi r\rho_0[\rho(r)/\rho_o - 1]$, which is the formal definition of the PDF $G(r)$. High-energy synchrotron XRD and atomic PDFs have already proven to be very efficient in studying the atomic-scale structure of nanosized particles.[36]

X-ray Absorption Fine Structure (XAFS) Spectroscopy. Pt L3 edge (11 564 eV) and Co K edge (7709 eV) XAFS spectra were collected on the insertion device beamline of the Materials Research Collaborative Access Team (MRCAT) at the Advanced Photon Source, Argonne National Laboratory. A cryogenic double-crystal Si(111) monochromator was used along with a Rh-coated mirror to reduce harmonics. All spectra were collected in transmission mode. Powder samples were pressed into pellets with a proper thickness to ensure a good quality of the data. A metal cell with open parallel channels 4 mm in diameter was used. A proper amount of sample was pressed into a self-supporting pellet inside the channel using a pair of dies. X-ray intensity before and after the pellet samples was measured by ionization chambers filled with N_2. In addition, reference spectra of Pt or Co foils for energy calibration were collected simultaneously, with each scan using an additional ionization chamber. XAFS can be divided into two regions: near-edge region or X-ray absorption near edge structure (XANES) and extended region (EXAFS). A detailed description of XANES and EXAFS theory and data processing is provided elsewhere.[37] XANES spectra were processed using Athena.[38] EXAFS spectra were extracted using Athena, and fitting of EXAFS data was performed using Artemis.[38] Background removal and edge-step normalization were performed using the AUTOBK program.[38] FEFFIT[39] was then used to fit the EXAFS function using paths for Pt species (Pt−O, etc.) as generated by the FEFF code (version 6.0).[40] The fitting was limited to 2.0−16.0 Å^{-1} for the Pt L3 edge spectra and 2.0−14.0 Å^{-1} for Co K edge spectra, using a Hanning window of Δk = 1.0 Å^{-1}. The fits were performed to both the real and imaginary parts of $\chi(R)$ in the region of 1.0 < R < 3.2 Å. Similar analysis was performed on the reference samples of Pt and Co foils to obtain the so-called amplitude reduction factor, S_0^2, used in the subsequent determination of the Me−Me atom first coordination numbers.

Because of the similar atomic radius of Co and V (0.07 Å difference) and the similar atomic number of Co (27) and V (23), Pt edge EXAFS data were fitted with either O, Co, Pt (PtCo model) or O, V, Pt (PtV model) in the first coordination shell with the understanding that Pt−Co path in PtCo model or Pt−V path in PtV model is used to represent both Pt−Co and Pt−V scattering paths.

The nearest neighbors around Co may include O, Co, V, and Pt. Fittings of Co K-edge edge EXAFS data were attempted using O, Co, and Pt (CoCo model) or O, V, and Pt (CoV model) in the first coordination shell with the understanding that the Co−Co path in the CoCo model or Co−V path in the CoV model is used to represent both Co−Co and Co−V scattering paths in the samples. Similar to the fitting of Pt EXAFS data, the CoV model resulted in underestimated DWF (~4 × 10^{-3} Å^2). Thus, to fit Co K edge EXAFS data in this work, the CoCo model was used (Supporting Information Table S1).

X-ray photoelectron spectroscopy (XPS) measurements were performed to identify the oxidation states of Pt, V, and Co on the surface of the catalysts. The XPS measurements were obtained on a Physical Electronics 5000 versa probe scanning ESCA microprobe. The system uses a focused monochromatic Al Kα X-ray (1486.7 eV) source for excitation and a spherical section analyzer. The instrument has a 16-element multichannel detection system. The X-ray beam was 100 W in power and with a diameter of 200 μm. It was incident normal to the sample, and the X-ray detector was at 45° off the normal. Wide scan data were collected using a pass energy of 187.85 eV. The binding energy (BE) scale was calibrated using the Cu $2p_{3/2}$ line at 932.58 ± 0.05 eV and the Au $4f_{7/2}$ line at 84.01 ± 0.05 eV. The sample experienced variable degrees of charging by low-energy electrons at ~1.5 eV, 20 μA so that low-energy Ar^+ ions needed to be used to minimize this charging. The percentages of individual elements detected were determined from the relative composition analysis of the areas of the XPS lines.

Electrochemical measurements were performed using a micro-computer-controlled electrochemical analyzer (CHI 620A, CH Instruments). The experiments were performed in three-electrode electrochemical cells at room temperature. All electrolytic (0.1 M $HClO_4$) solutions were deaerated with high-purity nitrogen before the measurement for cyclic voltammetry (CV) or saturated with oxygen for rotating disk electrode (RDE) measurements. The potentials are given with respect to the reversible hydrogen electrode (RHE).

RESULTS AND DISCUSSION

Control of the Ternary Composition. The control of composition in the PtMM′ nanoparticles, where M = Co and M′ = V, was achieved by controlling the feeding ratio of the three metal precursors in the synthetic reaction solution. Figure 1 shows a representative set of composition data to illustrate

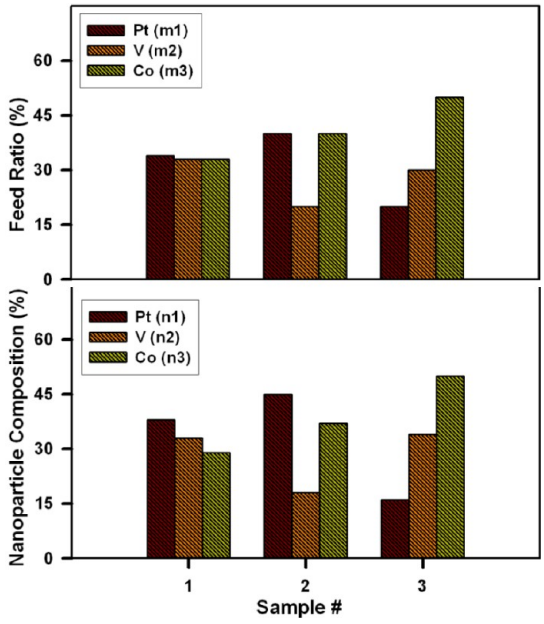

Figure 1. Comparison between the feed ratio ($Pt_{m1}V_{m2}Co_{m3}$, top panel) and the nanoparticle composition ($Pt_{n1}V_{n2}Co_{n3}$, bottom panel) for three typical synthesis batches (sample no.) targeting three different ternary compositions. Note that both the feeding ratio and the nanoparticles' composition are expressed as atom % for each metal.

dx.doi.org/10.1021/cm301613j | Chem. Mater. 2012, 24, 4283−4293

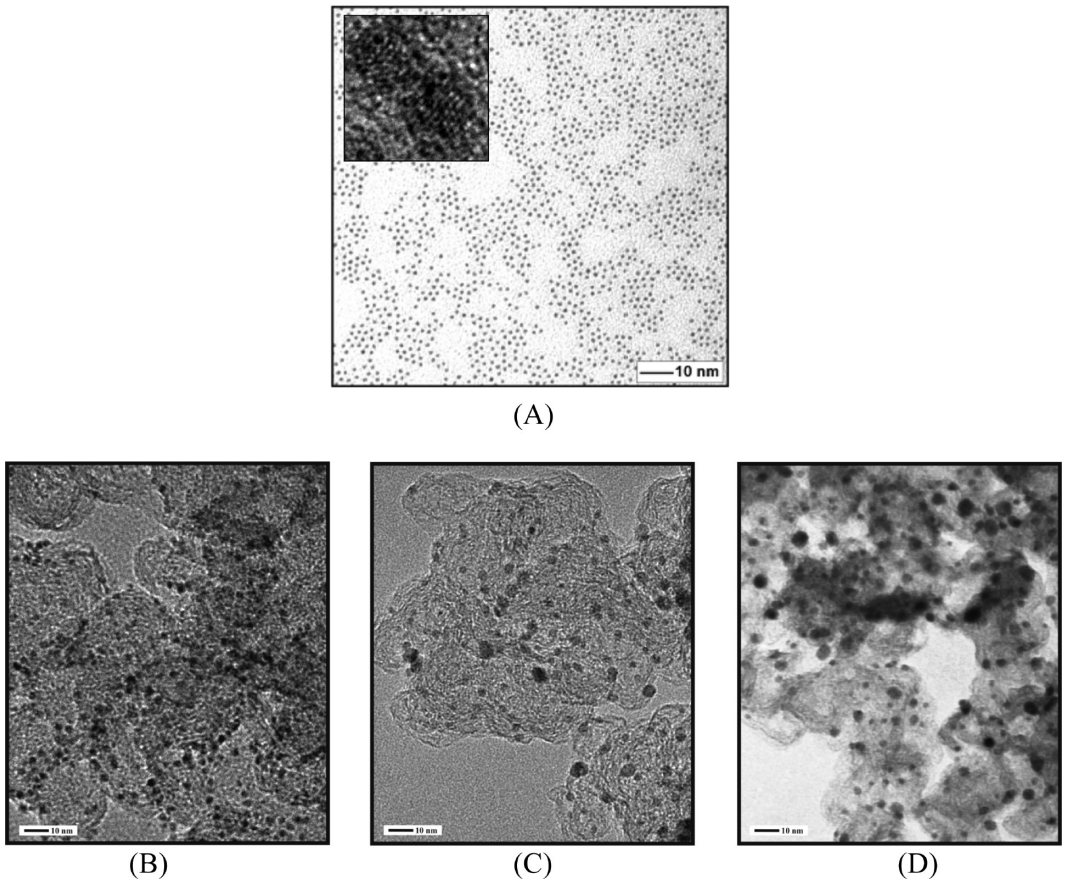

Figure 2. TEM micrographs for the as-synthesized $Pt_{45}V_{18}Co_{37}$ nanoparticles (A, 2.9 ± 0.3 nm; inset: a HR-TEM image), and for $Pt_{45}V_{18}Co_{37}$/C catalysts after oxidative treatment under O_2 at 260 °C followed by thermal treatment under H_2 at 400 °C (B, 3.3 ± 0.7 nm), 600 °C (C, 4.4 ± 1.3 nm), and 926 °C (D, 4.3 ± 1.3 nm; this image was obtained on a Hitachi H-7000 (see the Experimental section)). See Supporting Information Figure S1 for the size distributions.

the experimental correlation between the ternary feed ratio in the synthesis solutions and the ternary composition in the resulting PtVCo nanoparticles. It is evident that the correlation is quite good, demonstrating the controllability of the ternary composition by the synthesis technique in this work. Although the composition data are from bulk sample analysis, we believe that all the particles have basically similar composition and structure. This assessment is supported by the high monodispersity of the nanoparticles (Figure 2A) and the detailed analysis of a similar ternary nanoparticle system (PtVFe) synthesized by the same method[18,33] in which the high-resolution composition mapping of individual nanoparticles revealed almost identical composition for individual particles.

The size of as-synthesized ternary nanoparticles was controllable in terms of size monodispersity. For example, $Pt_{45}V_{18}Co_{37}$ nanoparticles showed an average size of 2.9 ± 0.3 nm (Figure 2A and Supporting Information Figure S1A). Nanoparticles of the other compositions also showed relatively high monodispersity (Supporting Information Figure S2). A detailed examination of $Pt_{45}V_{18}Co_{37}$ nanoparticles was performed as a representative system considering the fact that catalysts of this composition showed an intermediate catalytic activity.

To prepare catalysts, the as-synthesized ternary nanoparticles were supported on carbon in a controlled feed ratio, followed by thermochemical treatments. The actual loading of the alloys on the carbon support was determined by TGA. The thermochemical treatments involved a combination of thermal treatment, first under nitrogen ("N", minimum or nonreactive) or oxygen ("O"), followed by reductive treatment under hydrogen ("H"). Typically, the "N" or "O" treatment was performed at 260 °C, and the "H" treatment was performed at temperatures ranging from 400 to 926 °C. "N + H" stands for "N" treatment followed by "H" treatment. "O + H" stands for "O" treatment followed by "H" treatment. Figure 2 shows a representative set of TEM data to illustrate the particle size controllability of the catalysts. Catalysts after the combination of the oxidation−reductive treatments, that is, "O" followed by "H" treatments, with the latter conducted at temperatures ranging from 400 to 926 °C, showed a particle size increase from 3.3 ± 0.7 (400 °C) to 4.3 ± 1.3 nm (926 °C) (Supporting Information Figure S1).

While producing the apparent size change, the combination of "O" and "H" treatments has played an important role in the nanoscale alloying and structural/chemical ordering of the nanoalloys in maximizing the catalytic activity and stability, which are entailed in the next two subsections on the electrocatalytic activity and the structural properties,

Electrocatalytic Activities for ORR. The electrochemical activity of the PtVCo/C catalysts was found to depend on the atmosphere and temperature of the post synthesis treatment. As an example, we show CV measurements for $Pt_{45}V_{18}Co_{37}$/C catalysts subjected to "N + H" and "O + H" treatments at 400

dx.doi.org/10.1021/cm301613j | *Chem. Mater.* 2012, 24, 4283−4293

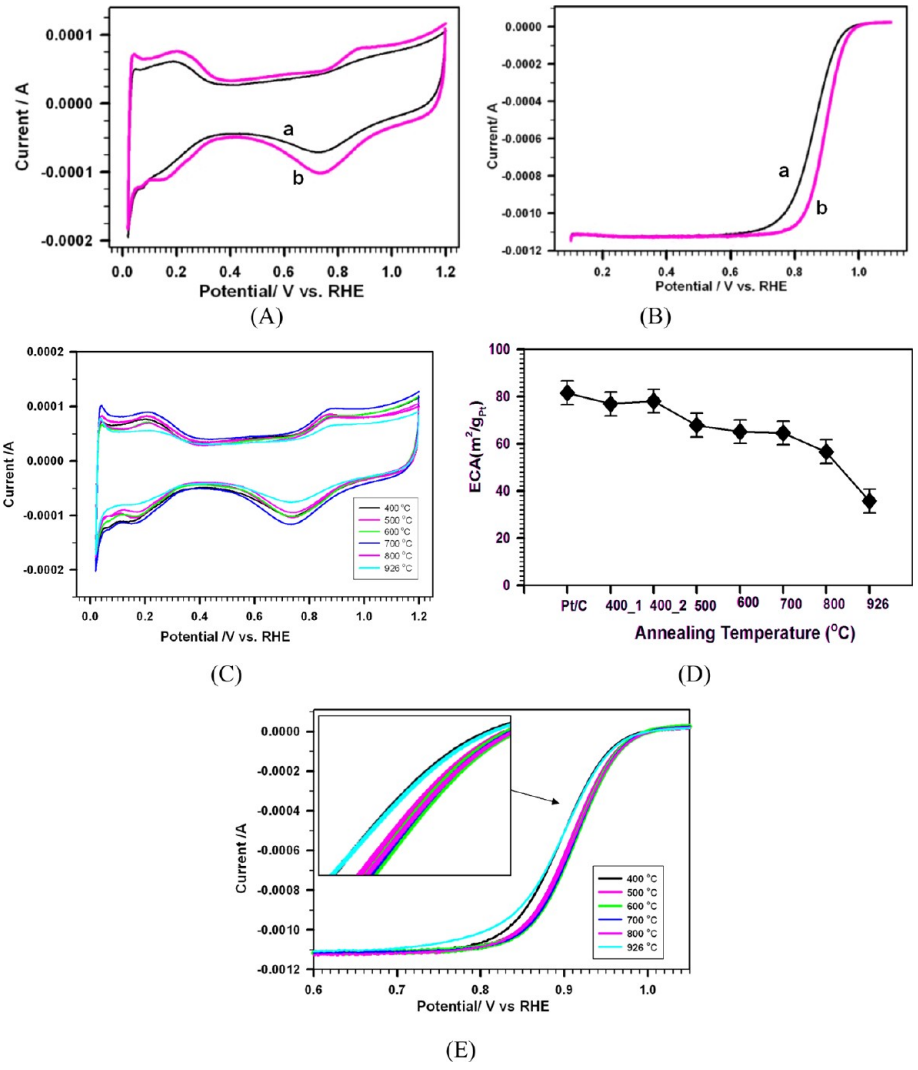

Figure 3. (A, B) CV and RDE curves for $Pt_{45}V_{18}Co_{37}$/C (20% loading) catalysts subjected to "N + H" (a) and "O + H" (b) treatments at 400 °C. (A) CV curves in N_2-saturated 0.1 M $HClO_4$. Scan rate: 50 mV/s. (B) RDE curves in O_2-saturated 0.1 M $HClO_4$. Scan rate: 10 mV/s at 1600 rpm. (C) CV curves for the $Pt_{45}V_{18}Co_{37}$/C catalysts subjected to "O + H" treatments at different temperatures (400, 500, 600, 700, 800, and 926 °C). Electrolyte: N_2-saturated 0.1 M $HClO_4$. Scan rate: 50 mV/s. (D) Plot of ECA values vs the annealing temperature. (E) RDE curves for the same catalysts annealed at different temperatures (inset: a zoomed view of the kinetc current region). Electrolyte: O_2-saturated 0.1 M $HClO_4$. Scan rate: 10 mV/s at 1600 rpm (catalyst loading = 10 μg on a GC electrode (0.196 cm^2)).

°C (Figure 3A). In contrast to the relatively featureless behavior of the "N + H"-treated sample, the hydrogen adsorption/desorption peaks at ~0.20 V become predominant for the "O + H"-treated samples, whereas the electrochemical active area (ECA) was found to be the same for both "N + H"-treated (76.79 m^2/g_{Pt}) and "O + H"-treated (77.98 m^2/g_{Pt}) samples. In the kinetic region of the RDE curves for ORR (Figure 3B), there is a clear indication of an increased kinetic current for the "O + H"-treated catalysts. From these data, a mass activity (MA) value of 0.25 A/mg_{Pt} was found for the "N + H" catalyst, which was much smaller than that for the "O + H" catalyst (0.62 A/mg_{Pt}).

For samples annealed at 400−700 °C, the hydrogen adsorption/desorption peak at ~0.20 V becomes predominant but diminishes upon further annealing at 926 °C. The ECA values (Figure 3C and D) showed a gradual decrease upon increasing the temperature to 700 °C and a significant decrease above 800 °C. In the kinetic region of the RDE curves (Figure 3E), there is a clear signature of an initial increase in the current with an increase in the annealing temperature until 600 °C, after which the current decreases.

Both the mass activity and specific activity (SA) were directly determined from the kinetic current in the RDE curves. As shown in Figure 4, both the mass activity and specific activity of the H_2-treated catalysts increase significantly with the annealing temperature as compared with the commercial Pt/C catalyst and the only "N_2"-treated catalysts. There is a clear trend of increasing the mass activity with the annealing temperature until it reaches a maximum at 600 °C. The specific activity also shows a similar maximum with an increase in the annealing temperature. Both the mass and specific activities clearly maximize at an annealing temperature close to 600 °C.

Note that the above mass activity data were obtained without subjecting to IR drop correction, as done in some recent reports on PtNi catalysts,[41] and on PtCo catalysts,[13] for which the mass activity data given were extracted after a correction of the IR drop in the RDE curves.[42] In most of the literature, the activity data were obtained from RDE without performing the

dx.doi.org/10.1021/cm301613j | Chem. Mater. 2012, 24, 4283−4293

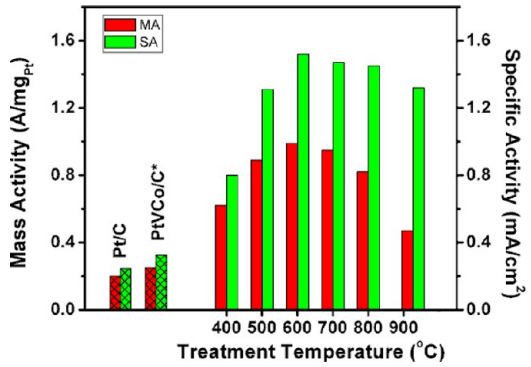

Figure 4. Plots of the mass (red, error ±4%) and specific activity (green, error ±8%) at 0.9 V (vs RHE) for $Pt_{45}V_{18}Co_{37}$/C catalysts subjected to "O + H" treatment at different temperatures. Data for the catalyst treated by "N + H" at 400 °C (PtVCo/C*) and a commercial Pt/C catalyst are included for comparison.

IR drop correction.[17,18,22−28,43−46] It is known that the "IR drop"-corrected mass activity is higher than that without IR drop correction.[42] As shown in the Supporting Information (Figure S3), for a comparison of RDE curves with and without IR drop correction for a catalyst with the highest mass activity in our manuscript (i.e., the 600 °C-catalyst in Figure 3), the RDE curve is shifted to a higher potential after the IR drop correction, from which the extracted mass activity is 3.3 A/mg Pt, 3.3 times larger than the mass activity data reported in Figure 4.

The observation of a clear peak in the catalytic activity as a function of the particle's annealing temperature is, to the best of our knowledge, the first example for ternary PMM′ catalysts. Previous studies on PMM′ catalysts have found only a gradual increase in this temperature range.[27] This finding cannot be explained in terms of particle's size effect, since the particle's size just smoothly increases with the temperature of annealing. Neither can it be explained in terms of the ECA effect, since the ECA decreases gradually with the annealing temperature. To gain a better understanding, three closely related physical and chemical properties were examined, including the degree of chemical alloying, the Pt-transition metal coordination structure, and the surface composition of the nanocatalysts, as described below.

Structures of the Ternary Nanoalloys. XRD patterns for the as-synthesized nanoparticles (A) and the catalysts treated at 400 °C under N_2 and O_2 (B) are shown in Figure 5. Note that for the $Pt_{45}V_{18}Co_{37}$ nanoparticles, the Bragg peaks are very broad. In addition, the "N + H"-treated catalysts showed broad and very poorly resolved XRD peaks, indicating a low degree of crystallinity or rather small particle size (or both), whereas the "O + H"-treated catalysts show much sharper XRD peaks, indicating a much higher degree of crystallinity or larger particle size. There is no indication of the presence of secondary phases of the individual metals.

Figure 6 shows a typical set of in-house XRD patterns for the $Pt_{45}V_{18}Co_{37}$/C catalysts after an oxidative treatment under O_2 followed by reductive annealing under H_2 at different temperatures ("O + H"). A closer look at the XRD patterns (Figure 6), however, suggests the structural evolution for the catalysts treated in "O + H" atmosphere may not be explained in terms of an fcc-type structure alone. The catalysts remain single-phase materials and become more crystalline in nature. In addition, the shift in Bragg peaks indicates a shortening of the interatomic distances. This is evidenced qualitatively by the XRD patterns in Figure 6. First, as the temperature increases, the peaks become narrower and fall between those for Pt and for the alloyed base metals (Figure 6A), indicating a single-phase characteristic. There is a subtle increase in the particle size with an increased crystalline feature with the increase in temperature; however, the size increase appears to be small from the TEM data, which level off at 600−700 °C.

A slightly larger increase in particle sizes but with similar trend is also observed from the data estimated using the Scherrer equation (Figure 6B, and also the Supporting Information). Second, there is an increase in the Bragg peak position, from which the hypothetical fcc lattice inferred from the major Bragg peaks showed a gradual decrease (Figure 6B). Note that the degree of alloying is defined by both chemical and structural ordering of the metal components. Chemically, a random alloy has the highest degree of alloying because the metal atoms of different components are fully mixed. Structurally, it is the structure type (e.g., fcc or fct type for the catalysts studied in this paper) and interatomic distances (e.g., fcc- or fct-type lattice constant) that determine the degree of alloying. For the metals studied in this work, a shorter lattice distance is associated with a higher degree of alloying.

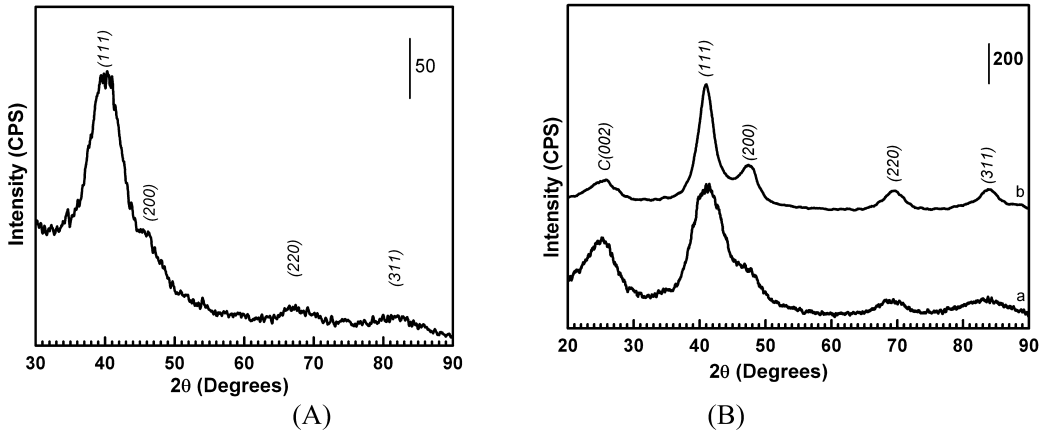

Figure 5. XRD patterns for (A) as-synthesized $Pt_{45}V_{18}Co_{37}$ nanoparticles, and (B) $Pt_{45}V_{18}Co_{37}$/C catalysts after thermal treatment under N_2 (a) and O_2 (b) followed by reductive annealing under hydrogen at 400 °C (the intensity bar (counts) is indicated in the upper-right corner).

dx.doi.org/10.1021/cm301613j | Chem. Mater. 2012, 24, 4283−4293

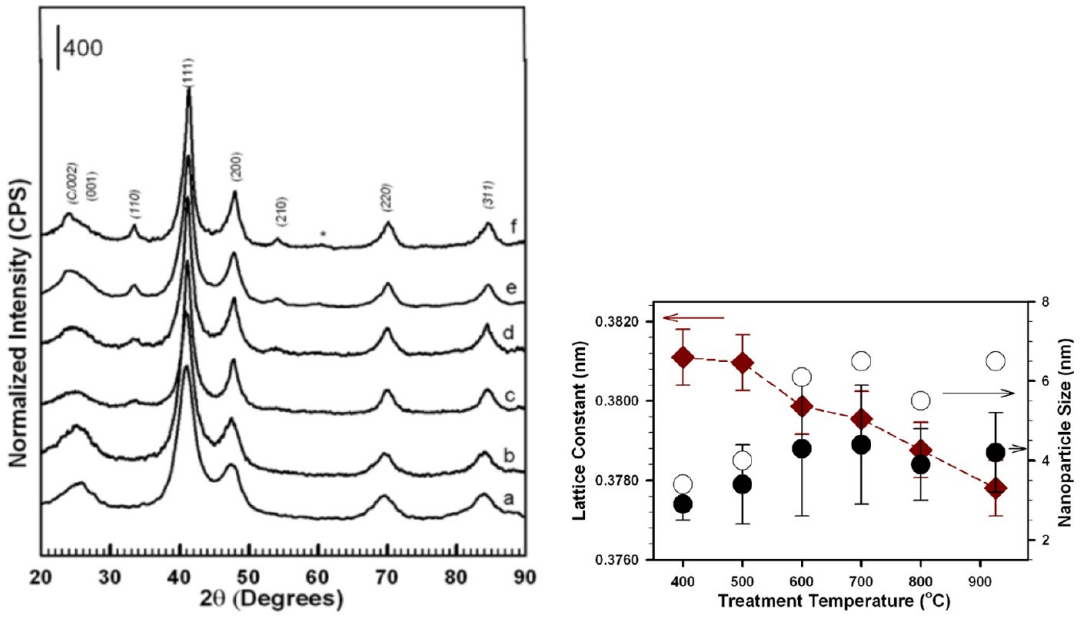

Figure 6. (A) In-house XRD patterns for $Pt_{45}V_{18}Co_{37}/C$ catalysts after thermal treatment under O_2, followed by reductive annealing under hydrogen at temperatures (a) 400, (b) 500, (c) 600, (d) 700, (e) 800, and (f) 926 °C (the intensity bar (counts) is indicated in upper-left corner). (B) Plots of the lattice parameter (diamonds) of a hypothetical fcc lattice inferred from the major Bragg peaks and the particle sizes (solid (from TEM) and open (from XRD) circles, respectively) vs temperature. Low-intensity extra peaks appearing at >600 °C may be indexed as (100), (001), (200), (002), and (110) Bragg peaks from an fct lattice.

If the XRD data for all "O + H"-annealed samples are considered in terms of an fcc structure and its lattice parameter is evaluated, that parameter shows a contraction with the annealing temperature from 0.3826 nm (for 400 °C) to 0.3797 nm (for 926 °C). This contraction is an indicator of the shrinking of the interatomic distances, that is, of an increased packing density of the metal atoms inside the particles with an increase in the annealing temperature. The appearance of extra, low-intensity peaks for the samples annealed at T > 600 °C, however, clearly shows that the particle's structure rearranges away from the fcc type at higher temperatures. This rearrangement transforms the fcc–type structure of the as-prepared and annealed up to 400 °C particles into particles with a face-centered tetragonal (fct)-type structure.[47] A similar structural phase transition has been observed in binary alloy particle, such as PtCo and PtV.[30,48,49] There were also some early studies of the ternary systems (e.g., ref 50).

To reveal the nature of the atomic ordering in $Pt_{45}V_{18}Co_{37}/C$ and its temperature-driven evolution in more detail, we conducted HE-XRD experiments coupled to atomic pair distribution functions (PDF) analysis that is very well suited for nanosized particles.[49,51] HE-XRD patterns for $Pt_{45}V_{18}Co_{37}/C$ catalysts annealed at 400, 600, and 926 °C are shown in Figure 7. Atomic PDFs extracted from the HE-XRD patterns are shown in Figure 8 together with that for pure Pt particles used here as a standard. The PDFs exhibit a series of well-defined peaks reflecting the presence of a sequence of well-defined coordination spheres in the ternary catalysts. In the PDFs, for pure Pt particles, the first peak is positioned at 2.76(1) Å, which is very close to the Pt–Pt distance in the respective bulk metal. The first peak in the experimental PDFs of $Pt_{45}V_{18}Co_{37}/C$ particles is positioned at 2.70(1) Å, indicating a shortening of the metal–metal distances in the alloy particles as a result of the smaller size of the Co/V atoms as compared

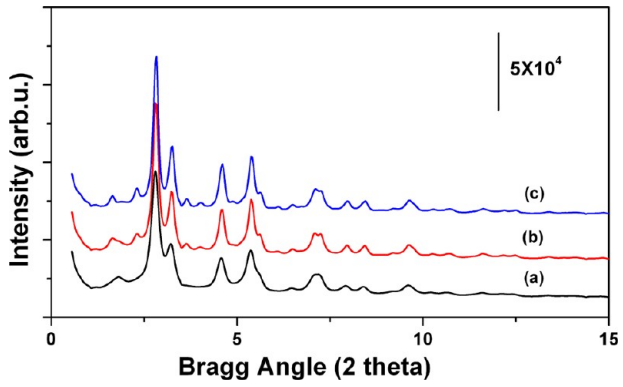

Figure 7. HE-XRD intensity patterns for $Pt_{45}V_{18}Co_{37}/C$ catalysts as a function of treatment temperature: (a) 400, (b) 600, and (c) 926 °C. Energy of X-rays: 115 keV (λ = 0.1078 Å) (the intensity bar (counts) is indicated in the upper-left corner).

with Pt atoms. All features in the PDF for pure Pt can be very well fit with a structure model featuring an fcc-type structure with a parameter of 3.92 Å. The PDF for the sample treated at 400 °C can be equally well described with structure models featuring a random PtVCo alloy fcc-type (R_w = 19%) or chemically ordered alloy fct-type (R_w = 18%) structure. The chemically ordered fct lattice model, however, becomes increasingly a better match to the experimental PDFs for the particles annealed at >400 °C (see comparison of the R_w's). Indeed, only the fct-type model can explain well the fine features of the experimental PDF data (see the encircled region) that are characteristic benchmarks of a chemically ordered structure in which Pt, Co, and V atoms are not randomly distributed within the nanoparticles but assume preferential ordering with respect to each other.

dx.doi.org/10.1021/cm301613j | Chem. Mater. 2012, 24, 4283–4293

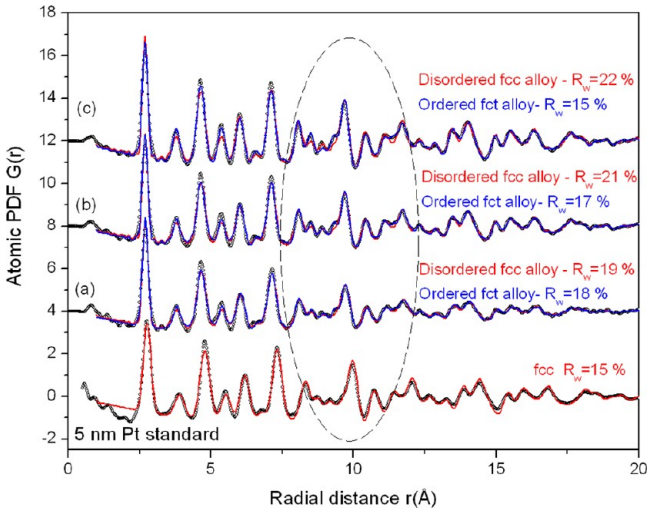

Figure 8. Atomic PDFs extracted from the HE-XRD diffraction patterns (Figure 6) for $Pt_{45}V_{18}Co_{37}$/C catalysts at annealing temperatures (a) 400, (b) 600, and (c) 926 °C. The PDF for 5 nm Pt particles is shown for comparison. Experimental PDFs (symbols) and model fits (line) that are based on structure models featuring chemically disordered fcc type (in red) and chemically ordered fct type (in blue) structure. Broken line encircles peaks that are increasingly better described in terms of an fct-type model with increasing temperature. The goodness-of-fit indicators, R_w, for each of the fits provides a measure of the difference between the model computed and the experimental PDF data.

The PDF refined fct lattice parameters change from a = 2.710 Å and c = 3.776 Å for the sample annealed at 400 °C to a = 2.700 Å and c = 3.773 Å at 600 °C and then to a = 2.698 Å and c = 3.770 Å at 926 °C. If Pt and $Pt_{45}V_{18}Co_{37}$ samples are compared on the basis of a hypothetical fcc model, the respective lattice parameters change from a = 3.82 Å (400 °C) to a = 3.809 Å (600 °C) and then to a = 3.803 Å (926 °C). In line with the in-house XRD data, the synchrotron-based PDF studies unambiguously show that with an increase in the temperature of annealing, (i) the $Pt_{45}V_{18}Co_{37}$/C catalysts undergo a phase transition from a random alloy to a chemically ordered alloy type structure (ii) accompanied by a shrinking of the distances between the metal atoms. The trend in these structural features nicely correlates with the increase of MA and SA with the annealing temperature, reaching a maximum at 600 °C. Above 600 °C, the subtle leveling off in the SA value and the slight drop in the MA value likely indicates that the further increase in the chemical ordering and shrinking in interatomic distances has little or even a detrimental effect on the activity enhancement. This is understandable because the adsorption and activation of molecular oxygen requires an optimal structure of the alloyed Pt sites.

Structural information about the atomic coordination between metals in $Pt_{45}V_{18}Co_{37}$/C catalysts was also obtained by EXAFS studies[26] on selected samples annealed at 400 and 800 °C. The understanding of the structural changes between these two temperatures provides additional information for assessing how the activity change with annealing temperature is related to the structural change of the catalysts.

Individual fitting of the Pt EXAFS data using the PtCo and PtV models was performed. The PtV model resulted in an underestimated DWF (~3 × 10^{-3} Å^2) for the Pt−Co/V path (even smaller than that of Pt−Pt, 6 × 10^{-3} Å^2), which is a result of fitting the Pt−Co path using Pt−V, as can be shown by a model experiment that was designed to evaluate the impact of using Pt−V to fit the Pt−Co scattering path (see Supporting Information Figure S4). In this work, the PtCo model is thus used for the fitting of Pt L3-edge EXAFS data. Figure 9 shows a set of EXAFS spectra data for the Pt L3 edge. The fitted bond distance and bond disorder for a specific neighbor (e.g., O, Co, Pt) are basically the same (or not significantly different) (Table 1 and Supporting Information Table S1), leaving the main difference in the coordination numbers. A fit with an apparently smaller DWF of Pt−Co/V than that of Pt−Pt is considered "unreasonable". Our fitting results not only show that there are more Pt−Co bonds than Pt−V bonds but also suggest that there are few Pt−V bonds in the system. Note that this type of fitting has been shown to be an effective way to reduce uncertainties associated with the fitted parameters.[25]

As summarized in Table 1 for the structural parameters from fitting Pt L3 edge EXAFS data using the PtCo model and the Co K edge data using the CoCo model for the $Pt_{45}V_{18}Co_{37}$/C catalyst, the results clearly show a significant presence of Co/V neighbors around Pt and Pt neighbors around Co, which is direct evidence of the formation of PtVCo alloy in the samples studied here. In addition, the EXAFS data (see Supporting Information Tables S1−2) indicate a higher probability of Pt bonding with transition metal atoms for the catalyst treated at 800 °C, as compared with the catalyst treated at 400 °C. For example, the coordination number (CN) of Pt−Co/V atomic pairs changes from 2.3 for the 400 °C-treated sample to 3.1 for

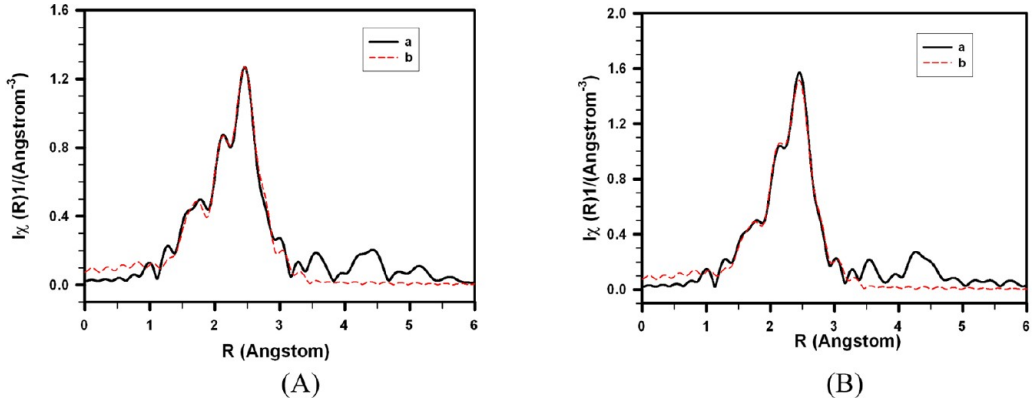

Figure 9. Original (a, black curve) and fitted (b, red curves) magnitudes of Fourier-transformed k^2-weighted Pt L3 edge EXAFS spectra of $Pt_{45}V_{18}Co_{37}$/C annealed at (A) 400 and (B) 800 °C using the Pt−Co model.

dx.doi.org/10.1021/cm301613j | Chem. Mater. 2012, 24, 4283−4293

Table 1. Structural Parameters from Fitting Pt L3 Edge EXAFS Data Using the Pt−Co Model and Co K Edge Data Using the Co−Co Model for $Pt_{45}V_{18}Co_{37}$/C Catalysts[a]

sample	scat path	*N*	*R* (Å)	DWF (10^{-3} Å^2)
		Pt L3 Edge		
400 °C	Pt−O	0.5 ± 0.1	1.99 ± 0.03	1.5 ± 2.8
	Pt−Co/V	2.3 ± 0.7	2.64 ± 0.01	8.9 ± 2.6
	Pt−Pt	5.7 ± 0.7	2.70 ± 0.01	6.7 ± 0.6
800 °C	Pt−O	0.4 ± 0.1	1.99 ± 0.03	1.5 ± 2.8
	Pt−Co/V	3.1 ± 0.5	2.64 ± 0.01	7.9 ± 1.3
	Pt−Pt	5.4 ± 0.6	2.69 ± 0.00	5.9 ± 0.5
		Co K Edge		
400 °C	Co−O	2.3 ± 0.3	1.99 ± 0.01	10.7 ± 2.4
	Co−Co/V	1.2 ± 0.5	2.62 ± 0.01	12.0 ± 5.1
	Co−Pt	4.1 ± 0.5	2.64 ± 0.01	9.1 ± 1.2
800 °C	Co−O	1.8 ± 0.2	1.99 ± 0.01	10.7 ± 2.4
	Co−Co/V	1.8 ± 0.8	2.62 ± 0.01	12.0 ± 5.1
	Co−Pt	4.9 ± 0.6	2.64 ± 0.01	9.1 ± 1. 2

[a]Note: *R* factor is 0.0088 for Pt L3 edges, 0.0127 for Co K edges. Scat path: scattering path. *N*: coordination number. *R*: bond length. DWF: Debye−Waller factor.

the 800 °C sample, whereas the corresponding change in CN of Pt−Pt is insignificant (from 5.7 to 5.4). Although an increase in the particle size may lead to an increase in the total CN, the more significant increase in CN of Pt−Co/V than that of Pt−Pt suggests better alloying between Pt and Co/V. The EXAFS results in Table 1 also indicate a clear reduction in the oxide content (e.g., reduction in the metal−oxygen CNs) for the 800 °C-treated sample. Although there is some difference in the mean values of CN(Pt−Co/V) and CN(Pt−Co) determined from CN(Co−Pt), there is no discrepancy in the result within the uncertainties. The conclusions drawn from the EAXFS analysis are based on both the mean values and the associated uncertainties.

The EXAFS data indicates significant Co (and V)-O but insignificant Pt−O coordination structures, suggesting the presence of oxygenated base metals in the nanoalloys. To determine whether the oxygenated metals are originating from the entire particle or the particle surface, the catalysts were also analyzed by XPS (Figure 10), which provides information about surface composition due to its surface sensitivity.[38] For the as-synthesized $Pt_{45}V_{18}Co_{37}$ nanoparticles, Pt $4f_{7/2}$ and $4f_{5/2}$ bands are observed at 71.7 and 75.6 eV. For the thermochemically treated catalysts, these two bands are observed at 71.9 and 75.2 eV (400 °C), 71.9 and 75.2 eV (600 °C), and 72.0, and 75.3 eV (800 °C). The V $2p_{3/2}$ peak is observed at 517.0 eV for the as-synthesized NPs and at 517.4 eV (400 °C), 517.5 eV (600 °C), and 517.6 eV (800 °C) for the treated catalysts. The Co $2p_{3/2}$ and $2p_{1/2}$ bands appear at 780.7 and 796.0 eV for the as-synthesized NPs and at 780.7 and 796.4 eV (400 °C), 780.7 and 796.1 eV (600 °C), and 780.6 and 796.1 eV (800 °C) for the treated catalysts. In the O1s region, there is also a slight shift in the BE from the as-synthesized NPs (531.9 eV) to a higher BE (532.1, 532.0, and 532.6 eV for the catalysts treated

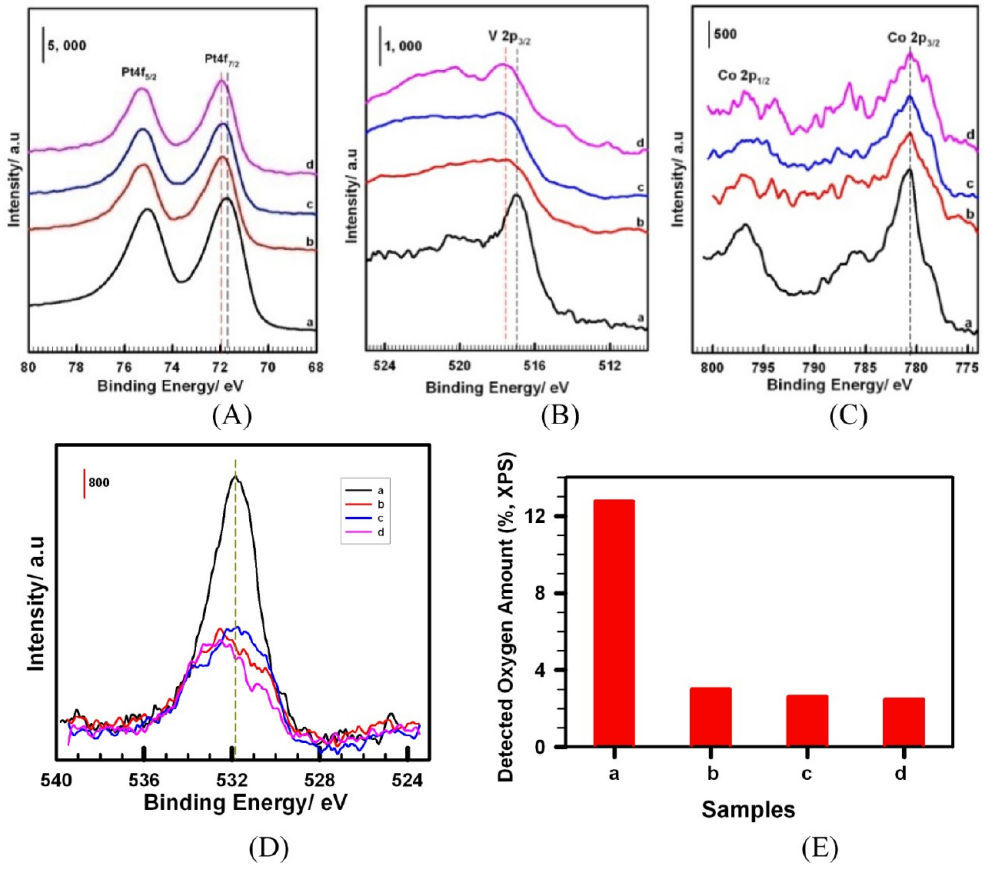

Figure 10. XPS spectra in the Pt4f (A), V2p (B), Co 2p (C), and O1s (D) regions for (a) samples of as-synthesized $Pt_{45}V_{18}Co_{37}$ nanoparticles and $Pt_{45}V_{18}Co_{37}$/C catalysts annealed at (b) 400, (c) 600, and (d) 800 °C. The bar chart plot (E) shows the detected oxygen percentages for these samples (the intensity bar (counts) is indicated in upper-left corner).

dx.doi.org/10.1021/cm301613j | *Chem. Mater.* 2012, 24, 4283−4293

at 400, 600, and 800 °C, respectively). By comparing the binding energies for Pt $4f_{7/2}$ and $4f_{5/2}$, V $2p_{3/2}$, and Co $2p_{3/2}$, and $2p_{1/2}$ for the supported catalysts annealed at different temperatures, and small or insignificant changes in the overall composition were observed in comparison with the as-synthesized particles. The small BE shift of Pt 4f7/2 to a higher BE value was not due to oxidation of Pt; rather, it was due to an increased degree of alloying of Pt with the base transition metals, which have a propensity of surface oxidation.

However, the relative surface composition of the supported particles was found to vary to some extent with the annealing temperature. For example, the surface compositions for the catalysts treated at 400, 600, and 800 °C were Pt(57)V(9)-Co(34), Pt(67)V(9)Co(24), and Pt(59)V(17)Co(24), respectively, indicating a considerable rearrangement of the chemical species within the particles upon annealing. This finding is consistent with the XRD/PDF findings of a chemical disorder−order phase transformation. The subtle difference of these surface compositions from their bulk compositions, Pt(48)-V(20)Co(32) (400 °C), Pt(52)V(17)Co(31) (600 °C), and Pt(50)V(17)Co(33) (800 °C), indicates a nonuniform distribution of the components in the particles; in particular, an enrichment of Pt on the surface. This enrichment may partially reflect unchanged ternary skeleton by the formation of the oxygenated base metals on the surface, as indicated by the decreased surface composition of the base metals. Interestingly, in comparison with the relative surface enrichment of Pt at the expense of V for 400 °C and Co for 800 °C, the observation of the surface enrichment of Pt at the expense of both V and Co at 600 °C may be an important clue for understanding the maximum catalytic activity of the catalyst treated at 600 °C. On the other hand, in contrast to the high percentage of the detected oxygen species for the as-synthesized nanoparticles, which originates largely from the capping molecules, the detected oxygen species for the treated catalysts are smaller but evidently at a higher BE, consistent with those for metal oxide species. The percentage of the oxygenated species shows a gradual decrease with the treatment temperature. This trend is consistent with the trend observed for the reduction of Co(V)−O coordination numbers with the treatment temperature (see Table 1), indicating the surface nature of the oxygenated base metal species. The synergistic effect of oxygenated V and Co species on the surface may be responsible in part for the structural perfection of the as-prepared catalysts. The details will be further investigated by in situ HE-XRD/PDFs and in situ XAFS characterizations, which are part of our ongoing work.

CONCLUSIONS

In conclusion, the nanoscale alloying and structural perfection through the oxidative−reductive thermochemical treatments is shown to produce a significant enhancement in electrocatalytic activity of the ternary nanoalloy catalysts for oxygen reduction reaction. The structure of the ternary nanoalloy of Pt with V and Co under the controlled oxidative−reductive thermochemical treatment is driven from a chemically disordered state into a chemically ordered state with an enhanced degree of alloying, demonstrating an excellent example of how the nanoscale structural and chemical ordering influences the electrocatalytic properties. This insight highlights the importance of atomic-scale structural and chemical ordering evolution in nanoalloy catalysts and the proper use of HE-XRD/PDF and EXAFS techniques to reveal such detailed changes. In the nanoparticles, Pt and Co/V are randomly alloyed in an fcc-type structure. Upon increasing the annealing temperatures, (i) the degree of the structural order increases, (ii) the interatomic distances shrink, and (iii) Pt and Co/V species rearrange in a chemically ordered fct type structure, leading to an enhanced catalytic activity for ORR. The further increase in the degree of chemical and structural ordering at annealing temperatures higher than 600 °C has little or even a detrimental effect on the activity enhancement, implying the existence of an optimal structure of the alloyed Pt sites for the adsorption and activation of molecular oxygen. Note that under the ORR operation conditions, the base metals (V and Co) on the surface of the ternary nanoalloy would likely dissolve into the acidic electrolyte,[4−6] leaving a Pt-rich surface behind. However, it is the structural and chemical ordering in the nanoalloy particle perfected by the oxidative−reductive thermal annealing that has determined the surface structure of the nanoalloy catalyst under ORR conditions for the enhanced activity. For further understanding of the nanoalloy structural evolution in correlation with the catalytic activity, in situ synchrotron X-ray studies of the thermochemical treatment under controlled atmosphere and the electrochemical process under fuel-cell operation conditions are part of our ongoing investigation.

ASSOCIATED CONTENT

Supporting Information

Additional experimental data (PDF). This information is available free of charge via the Internet at http://pubs.acs.org/.

AUTHOR INFORMATION

Corresponding Author

*E-mail: cjzhong@binghamton.edu.

Notes

The authors declare no competing financial interest.

ACKNOWLEDGMENTS

This work was supported by UTC Power, the NSF (CBET-0709113, and in part by CHE-0848701 and CMMI 1100736), and the DOE-BES Grants (DE-SC0006877). MRCAT operations are supported by the Department of Energy and the MRCAT member institutions. Use of the Advanced Photon Source is supported by the Office of Basic Energy Sciences of the U.S. Department of Energy under Contract No. W-31-109-Eng-38. We thank M. Engelhard for XPS measurement at EMSL, a national scientific user facility sponsored by the DOE located at PNNL, and Dr. O. Malis for helpful discussions on earlier XRD data.

REFERENCES

(1) Zhong, C. J.; Luo, J.; Njoki, P. N.; Mott, D.; Wanjala, B.; Loukrakpam, R.; Lim, S.; Wang, L.; Fang, B.; Xu, Z. C. *Energy Environ. Sci.* **2008**, *1*, 454.

(2) Jalan, V.; Taylor, E. J. *J. Electrochem. Soc.* **1983**, *130* (11), 2299.

(3) Mukerjee, S.; Srinivasan, S.; Soriaga, M. P.; McBreen, J. *J. Phys. Chem.* **1995**, *99* (13), 4577.

(4) Stamenkovic, V. R.; Fowler, B.; Mun, B. S.; Wang, G. F.; Ross, P. N.; Lucas, C. A.; Markovic, N. M. *Science* **2007**, *315* (5811), 493.

(5) Stamenkovic, V.; Mun, B. S.; Mayrhofer, K. J. J.; Ross, P. N.; Markovic, N. M.; Rossmeisl, J.; Greeley, J.; Norskov, J. K. *Angew. Chem., Int. Ed.* **2006**, *45* (18), 2897.

(6) Chen, S.; Sheng, W. C.; Yabuuchi, N.; Ferreira, P. J.; Allard, L. F.; Shao-Horn, Y. *J. Phys. Chem. C* **2009**, *113* (3), 1109.

(7) Kinoshita, K. *J. Electrochem. Soc.* **1990**, *135*, 845.
(8) Sattler, M. L.; Ross, P. N. *Ultramicroscopy* **1986**, *20*, 21.
(9) Watanabe, M.; Saegusa, S.; Stonehart, P. *Chem. Lett.* **1988**, *9*, 1487.
(10) Bregoli, L. *Electrochim. Acta* **1978**, *23*, 489.
(11) Bett, J.; Lundquist, J.; Washington, E.; Stonehart, P. *Electrochim. Acta* **1973**, *18*, 343.
(12) Ruban, A. V.; Skriver, H. L.; Norskov, J. K. *Phys. Rev. B* **1999**, *59* (24), 15990.
(13) Wang, C.; van der Vilet, D.; Chang, K. C.; You, H. D.; Strmcnik, D.; Schlueter, J. A.; Markovic, N. M.; Stamenkovic, V. R. *J. Phys. Chem. C* **2009**, *113* (45), 19365.
(14) Lai, F.-J.; Sarma, L. S.; Chou, H.-L.; Liu, D.-G.; Hsieh, C.-A.; Lee, J.-F.; Hwang, B.-J. *J. Phys. Chem. C* **2009**, *113*, 12674.
(15) Landsman, D. A.; Luczak, F. J. U.S. Patent 4316944, 1982
(16) Gasteiger, H. A.; Kocha, S. S.; Sompalli, B.; Wagner, F. T. *Appl. Catal., B* **2005**, *56* (1−2), 9.
(17) Luo, J.; Wang, L. Y.; Mott, D.; Njoki, P. N.; Kariuki, N.; Zhong, C. J.; He, T. *J. Mater. Chem.* **2006**, *16* (17), 1665.
(18) (a) Luo, J.; Han, L.; Kariuki, N. N.; Wang, L. Y.; Mott, D.; Zhong, C. J.; He, T. *Chem. Mater.* **2005**, *17* (21), 5282. (b) He, T.; Kreidler, E.; Xiong, L.; Luo, J.; Zhong, C. J. *J. Electrochem. Soc.* **2006**, *153* (9), A1637.
(19) Stamenkovic, V. R.; Mun, B. S.; Mayrhofer, K. J. J.; Ross, P. N.; Markovic, N. M. *J. Am. Chem. Soc.* **2006**, *128* (27), 8813.
(20) Sethuraman, V. A.; Weidner, J. W.; Haug, A. T.; Pemberton, M.; Protsailo, L. V. *Electrochim. Acta* **2009**, *54* (23), 5571.
(21) Srivastava, R.; Mani, P.; Hahn, N.; Strasser, P. *Angew. Chem., Int. Ed.* **2007**, *46* (47), 8988−8991.
(22) Fang, B.; Luo, J.; Njoki, P. N.; Loukrakpam, R.; Mott, D.; Wanjala, B.; Hu, X.; Zhong, C. J. *Electrochem. Commun.* **2009**, *11* (6), 1139.
(23) Luo, J.; Wang, L.; Mott, D.; Njoki, P. N.; Lin, Y.; He, T.; Xu, Z.; Wanjala, B. N.; Lim, I. I. S.; Zhong, C. J. *Adv. Mater.* **2008**, *20* (22), 4342.
(24) Fang, B.; Luo, J.; Chen, Y.; Wanjala, B. N.; Loukrakpam, R.; Hong, J.; Yin, J.; Hu, X.; Hu, P.; Zhong, C. J. *ChemCatChem* **2011**, *3*, 583.
(25) Wanjala, B. N.; Fang, B.; Luo, J.; Chen, Y.; Yin, J.; Engelhard, M.; Loukrakpam, R.; Zhong, C. J. *J. Am. Chem. Soc.* **2011**, *133*, 12714.
(26) Wanjala, B. N.; Loukrakpam, R.; Lou, J.; Njoki, P. N.; Mott, D.; Zhong, C. J.; Shao, M.; Protsailo, L.; Kawamura, T. *J. Phys. Chem. C* **2010**, *114*, 17580.
(27) Loukrakpam, R.; Wanjala, B. N.; Yin, J.; Fang, B.; Luo, J.; Chen, Y.; Petkov, V.; Zhong, C. J.; Shao, M.; Protsailo, L.; Kawamura, T. *ACS Catal.* **2011**, *1*, 562.
(28) Loukrakpam, R.; Luo, J.; He, T.; Chen, Y.; Xu, Z.; Njoki, P. N.; Wanjala, B. N.; Fang, B.; Mott, D.; Yin, J.; Klar, J.; Powell, B.; Zhong, C. J. *J. Phys. Chem. C* **2011**, *115*, 1682.
(29) Antolini, E.; Passos, R. R.; Ticianelli, E. A. *Electrochim. Acta* **2002**, *48* (3), 263−270.
(30) Koh, S.; Leisch, J.; Toney, M. F.; Strasser, P. *J. Phys. Chem. C* **2007**, *111*, 3744.
(31) Ma, Y.; Balbuena, P. B. *J. Phys. Chem. C* **2008**, *112*, 14520.
(32) Greco, G.; Witkowska, A.; Minicucci, M.; Olivi, L.; Principi, E.; Dsoke, S.; Moretti, A.; Marassi, R.; Cicco, A. D. *J. Phys. Chem. C* **2012**, *116*, 12791.
(33) Zhong, C. J.; Luo, J.; Fang, B.; Wanjala, B. N.; Njoki, P. N.; Loukrakpam, R.; Yin, J. *Nanotechnology* **2010**, *21* (6), 20.
(34) Luo, J.; Kariuki, N.; Han, L.; Wang, L.; Zhong, C. J.; He, T. *Electrochim. Acta* **2006**, *51*, 4821.
(35) Petkov, V. *J. Appl. Crystallogr.* **1989**, *22*, 387.
(36) (a) Egami, T.; Billinge, S. J. L. *Underneath the Bragg peaks*; Pergamon Press: Amsterdam, 2003; (b) Petkov, V. *Mater. Today* **2008**, *11*, 28.
(37) Chen, Y. S.; Fulton, J. L.; Partenheimer, W. J. *J. Solution Chem.* **2005**, *34*, 993.
(38) Ravel, B.; Newville, M. *J. Synchrotron Radiat.* **2005**, *12*, 537.
(39) Newville, M. *J. Synchrotron Radiat.* **2001**, *8*, 322.
(40) Rehr, J. J.; Albers, R. C. *Rev. Modern Phys.* **2000**, *72*, 621.
(41) Wang, C.; Chi, M.; Li, D.; Strmcnik, D.; van der Vliet, D.; Wang, G.; Komanicky, V.; Chang, K. C.; Paulikas, A. P.; Tripkovic, D.; Pearson, J.; More, K. L.; Markovic, N. M.; Stamenkovic, V. R. *J. Am. Chem. Soc.* **2011**, *133* (36), 14396.
(42) van der Vliet, D.; Strmcnik, D. S.; Wang, C.; Stamenkovic, V. R.; Markovic, N. M.; Koper, M. T. M. *J. Electroanal. Chem.* **2010**, *647*, 29.
(43) Zhang, J.; Sasaki, K.; Sutter, E.; Adzic, R. R. *Science* **2007**, *315*, 220.
(44) Chen, S.; Gasteiger, H. A.; Shao-Horn, Y. *J. Electrochem. Soc.* **2010**, *157*, A82.
(45) Schulenburg, H.; Muller, E.; Khelashvili, G.; Roser, T.; Bonnemann, H.; Wokaun, A.; Scherer, G. G. *J. Phys. Chem. C* **2009**, *113*, 4069.
(46) Liu, Z.; Yu, C.; Rusakova, I. A.; Huang, D.; Strasser, P. *Top Catal.* **2008**, *49*, 241.
(47) Watanabe, M.; Tsurumi, K.; Mizukami, T.; Nakamura, T.; Stonehart, P. *J. Electrochem. Soc.* **1994**, *141* (10), 2659.
(48) Koh, S.; Yu, C.; Mani, P.; Srivastava, R.; Strasser, P. *J. Power Sources* **2007**, *172* (1), 50.
(49) Petkov, V. *Synchrotron Radiat. News* **2009**, *22*, 29.
(50) Luczak, F. J.; Landsman, D. A. U.S. Patent 4,677,092, 1987.
(51) Wanjala, B. N.; Luo, J.; Loukrakpam, R.; Fang, B.; Mott, D.; Njoki, P. N.; Engelhard, M.; Naslund, H. R.; Wu, J. K.; Wang, L. C.; Malis, O.; Zhong, C. J. *Chem. Mater.* **2010**, *22*, 4282.